

# mBEST: Realtime Deformable Linear Object Detection Through Minimal Bending Energy Skeleton Pixel Traversals

Andrew Choi<sup>1</sup>, Dezhong Tong<sup>2</sup>, Brian Park<sup>1</sup>,  
Demetri Terzopoulos<sup>1</sup>, Jungseock Joo<sup>3</sup>, and Mohammad Khalid Jawed<sup>†,2</sup>

**Abstract**—Robotic manipulation of deformable materials is a challenging task that often requires realtime visual feedback. This is especially true for deformable linear objects (DLOs) or “rods”, whose slender and flexible structures make proper tracking and detection nontrivial. To address this challenge, we present *mBEST*, a robust algorithm for the realtime detection of DLOs that is capable of producing an ordered pixel sequence of each DLO’s centerline along with segmentation masks. Our algorithm obtains a binary mask of the DLOs and then thins it to produce a skeleton pixel representation. After refining the skeleton to ensure topological correctness, the pixels are traversed to generate paths along each unique DLO. At the core of our algorithm, we postulate that intersections can be robustly handled by choosing the combination of paths that minimizes the cumulative bending energy of the DLO(s). We show that this simple and intuitive formulation outperforms the state-of-the-art methods for detecting DLOs with large numbers of sporadic crossings and curvatures with high variance. Furthermore, our method achieves a significant performance improvement of approximately 40 FPS compared to the 15 FPS of prior algorithms, which enables realtime applications.

## I. INTRODUCTION

As robots become increasingly more intelligent and capable, developing robust and effective deformable material manipulation skills has started to receive large research attention [1]. Among various deformable objects, deformable linear objects (DLOs) — typically referred to as “rods” by the mechanics community — are a special group, including everyday objects such as cables, ropes, tubes, and threads. Due to their unique geometric characteristic (width  $\sim$  height  $\ll$  length), DLOs are widely used in various domestic and industrial applications, including surgical suturing [2], knot fastening [3], [4], cable manipulation [5], [6], food manipulation [7], mechanics analysis [8], and more. However, because of their flexibility, DLOs are often prone to complex tangling, which complicates manipulation. In addition, the complicated structures made by DLOs usually have unique topology-induced mechanical properties [9]–[13] and are, therefore, used to tie knots

for sailing, fishing, climbing, and various other engineering applications. Given all of the above, a robust, efficient, and accurate perception algorithm for DLOs is crucial to both deformable material manipulation and soft robotics.

In this paper, we present an algorithm named *mBEST* (Minimal Bending Energy Skeleton pixel Traversals) for robust, accurate, and fast instance segmentation of DLOs. Without any prior knowledge regarding the geometries, colors, and total number of DLOs, *mBEST* takes a raw RGB image as input and provides a series of ordered pixels expressing the centerline of each unique DLO, thus allowing for the configurations of different DLOs to be easily incorporated into motion planning and manipulation schemes.

We implement the following sequence of processing procedures to achieve instance segmentation of DLOs. Like previous work [14], we first apply semantic image segmentation to achieve a binary mask of the DLOs against the background. We try two options for semantic segmentation. The first involves using a Deep Convolutional Neural Network (DCNN) segmentation model, resulting in binary masks of varying quality. The second is color filtering, which can achieve hyper-accurate binary masks but requires adequate color contrast between the DLOs and background. These two options are discussed in further detail in Sec. IV.

After a binary mask is achieved, we apply a thinning algorithm to the mask to obtain a skeleton pixel representation of the DLOs. The resulting representation preserves the connectivity and centerlines of the binary mask while being only a single pixel in width. Therefore, key points such as ends and intersections are easily detected. After a series of refinement steps to ensure topological correctness, the skeleton is then traversed, one end at a time, in a way that minimizes the cumulative bending energy of the DLOs until another end is encountered. Each traversal results in a unique DLO’s centerline pixel coordinates, which can then be used to optionally produce segmentation masks. Fig. 1 presents a high-level overview of the *mBEST* processing pipeline.

Overall, our main contributions in this article are to

- 1) develop a robust end-to-end pipeline for obtaining ordered centerline coordinates and segmentation masks of DLOs from images;
- 2) showcase that the relatively simple (and physically insightful) optimization objective of minimizing cumulative bending energy outperforms the state of the art (SOTA); and
- 3) achieve realtime performance that more than doubles the speed of the previous SOTA.

The authors are with the University of California, Los Angeles (UCLA), CA 90095, USA

<sup>1</sup>Andrew Choi, Brian Park, and Demetri Terzopoulos are with the UCLA Computer Science Department (email: asjchoi@cs.ucla.edu; brianpark@ucla.edu; dt@cs.ucla.edu)

<sup>2</sup>Dezhong Tong and Mohammad Khalid Jawed are with the UCLA Department of Mechanical & Aerospace Engineering (email: tlt1960308@g.ucla.edu; khalidjm@seas.ucla.edu)

<sup>3</sup>Jungseock Joo is with the UCLA Department of Communication and is currently working at NVIDIA Corporation (email: jjoo@comm.ucla.edu)

<sup>†</sup> Corresponding author.

This research was funded in part by the National Science Foundation under award numbers OAC-2209782, CMMI-2101751, CAREER-2047663, and IIS-1925360.

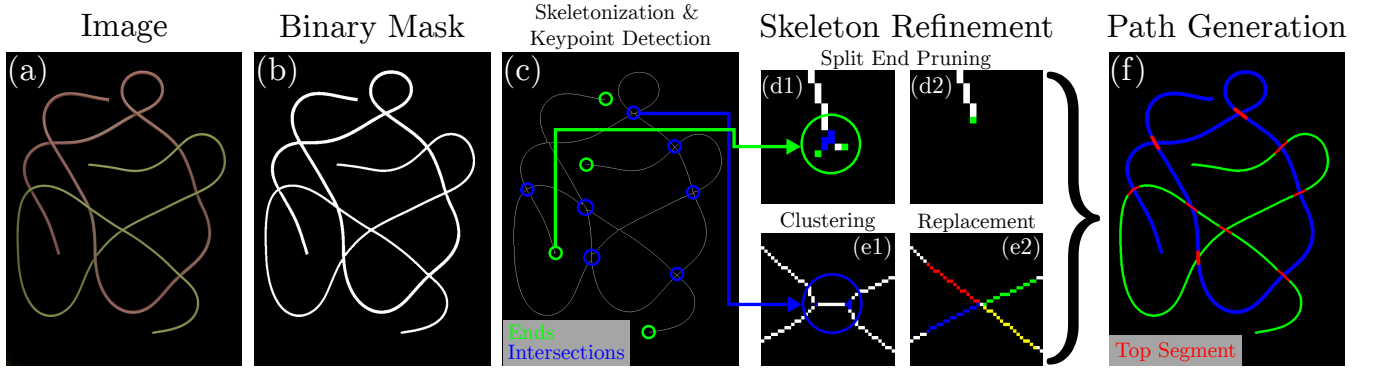


Fig. 1. Pipeline overview of *mBEST*. An input image (a) is converted to a binary mask (b) using a segmentation method. This binary mask is then converted to a skeleton pixel representation (c), where the connectivity and centerlines of the DLOs are preserved as a single-pixel-width structure, and keypoints such as intersections and ends are then detected. This is followed by a series of refinement steps to maintain the topological correctness of the skeleton: split ends (d1) are pruned (d2) and pixels representing a single topological intersection (e1) are clustered and replaced with a more intuitive intersection (e2). Finally, paths for each DLO are generated (f) by traversing skeleton pixels and choosing the path that minimizes cumulative bending energy.

In addition to the above, we release all the source code and datasets (with ground truth) used at <https://github.com/StructuresComp/mBEST>.

The remainder of the article is organized as follows: We proceed with a review of related work in Sec. II. The algorithmic formulation of *mBEST* is then discussed extensively in Sec. III. In Sec. IV, we report our experimental results comparing *mBEST* with SOTA approaches. Finally, we offer concluding remarks and discuss potential future research directions in Sec. V.

## II. RELATED WORK

Although research into developing manipulation skills for DLOs has been highly prevalent, the perception algorithms used in these efforts are usually undeveloped. For example, in the work of Tong et al. [8], attached markers are required for extracting the configuration of the manipulated DLO. Zhu et al. [5] carefully adjusted the workspace to increase the contrast between the manipulated DLO (cables) and their background. Although these prior efforts successfully completed their target manipulation tasks, the simplistic perception algorithms restrict real world applicability.

Consequently, DLO detection algorithms featuring various methodologies have been proposed. For example, Keipour et al. [15] evaluate both curvatures and distances to fit a continuous DLO. Using data-driven methods, Yan et al. [16] train a neural network to reconstruct the topology of a DLO based on a coarse-to-fine nodal representation. Though these methods achieve good results for some datasets, they work under the strict assumption that only one DLO exists within the scene, thus dramatically restricting their applicability.

One of the first perception algorithms capable of detecting multiple DLOs, *Ariadne* [17], segmented images into superpixels and traversed the superpixels belonging to DLOs in order to produce paths. The ambiguity of intersections is handled using a multi-faceted cost function that takes into consideration color, distance, and curvature. Despite its satisfactory performance, this early approach suffered from a large number of hyperparameters, an overreliance on DLOs

being a uniform color, and the tedious requirement on the user to manually select the ends of DLOs. Furthermore, the processing speed of *Ariadne* was on the order of seconds, precluding realtime operation.

In recent years, data-driven methods have attracted increasing attention in instance segmentation. In particular, researchers have shown that general instance segmentation problems can be tackled efficiently and accurately using Deep Convolutional Neural Networks (DCNNs) [18]–[21]. Furthermore, several tools have been introduced to help synthetically generate large quantities of photorealistic data in order to adequately train such models [22], [23]. Using DCNNs, Zanella et al. [24] created segmentations of DLOs such as wires; however, the segmentations did not distinguish between each DLO.

Improving upon *Ariadne*, *Ariadne+* [25], like [24], utilizes a DCNN model to extract an initial binary mask of the DLOs. This allows the algorithm to then apply superpixel segmentation purely on the binary mask itself, significantly reducing the computation time. Paths are then generated in a similar fashion to the original *Ariadne* algorithm by traversing superpixels while intersections are handled using a neural network to predict the most probable paths. The neural network uses the same three inputs as *Ariadne*: color, distance, and curvature. Despite these improvements, *Ariadne+* is sub-realtime; i.e., less than 3 FPS.

The state-of-the-art *FASTDLO* [14] improves upon *Ariadne+*’s speed by forgoing superpixel segmentation altogether. Instead, it uses a skeleton pixel representation of the DLO binary mask for path traversals. Intersections are then also handled by a neural network. By replacing superpixel segmentation with skeletonization, *FASTDLO* is reportedly able to achieve a realtime performance of 20 FPS for images of size  $640 \times 360$  pixels.

Though *Ariadne+* and *FASTDLO* are considered state-of-the-art DLO perception algorithms, both algorithms have been evaluated only on scenes with DLOs with relatively smooth curvatures and minimal self-loops. Our experiments will show that both algorithms struggle to solve complicated

TABLE I  
ALGORITHMIC COMPARISON

Algorithm	Intersection Rule	DLO Representation	Realtime
<i>Ariadne</i> [17]	color, distance, curvature	superpixels	✗
<i>Ariadne+</i> [25]	DNN prediction	superpixels	✓–
<i>FASTDLO</i> [14]	DNN prediction	skeleton pixels	✓
<i>mBEST</i>	curvature	skeleton pixels	✓

configurations (e.g., DLOs with highly variable curvatures resulting in many crossings and tangles) correctly.

By comparison, our *mBEST* robustly solves complex scenes using the simple notion that the most probable path is that which minimizes cumulative bending energy. Not only does it outperform the SOTA on complex scenes, but we also achieve realtime performance more than double that of *FASTDLO*. The key algorithmic differences between *mBEST* and the SOTA are summarized in Table I. Overall, we argue that the use of neural networks to solve intersections yields unsatisfactory results once input scenes stray away from the training data distributions, and we show that using a more principled formulation with physical insight can outperform black box neural network approaches for a wide variety of scenes containing DLOs.

### III. METHODOLOGY

Our algorithm may be divided into the following steps:

- 1) DLO Segmentation
- 2) Skeletonization
- 3) Keypoint Detection
- 4) Pruning Split Ends
- 5) Intersection Clustering and Replacement
- 6) Minimal Bending Energy Path Generation
- 7) Computing DLO Radii and Crossing Order

The following sections will describe each step in detail.

#### A. DLO Segmentation

The first step in detecting the DLOs is to obtain a binary mask  $\mathbf{M}_{\text{dlo}}$  of the image that distinguishes all DLO-related pixels from the background. As mentioned previously, we use two semantic segmentation methods: a DCNN segmentation model and color filtering. In particular, we use *FASTDLO*'s pretrained DCNN model [14] in our experiments. To eliminate noise, morphological closing and opening operations are performed on the binary mask to remove any hollow areas.

The initial semantic segmentation method is not a key contribution of *mBEST*. Rather, it is a modular component of the pipeline, allowing for different methods to be plugged in depending on the use case.

#### B. Skeletonization

The next step of the algorithm is to convert  $\mathbf{M}_{\text{dlo}}$  to a skeleton mask  $\mathbf{M}_{\text{sk}}$  as shown in Fig. 1(b-c).  $\mathbf{M}_{\text{sk}}$  is useful as both the connectivity and general topology of the DLOs are maintained. Furthermore, as segments are only 1 pixel in

width, traversals along segments are not susceptible to path ambiguity. To achieve skeletonization, we use an efficient thinning algorithm designed specifically for 2D images; refer to [26] for the details.

#### C. Keypoint Detection

Once a skeleton pixel representation is obtained, we can then detect two types of key points: ends and intersections. Locating ends is crucial as they serve as the start and finish points for skeleton pixel traversals. They also indirectly tell us the number of DLO(s) in the image as  $n_{\text{dlo}} = n_{\text{ends}}/2$  (assuming the initial binary mask maintained connectivity). Locating intersections is crucial as these represent the only points at which a pixel traversal will have multiple possible routes. Therefore, care must be given in choosing the correct path when passing through an intersection.

To detect ends and intersections, a skeleton pixel classification kernel,

$$\mathbf{K} = \begin{bmatrix} 1 & 1 & 1 \\ 1 & 10 & 1 \\ 1 & 1 & 1 \end{bmatrix},$$

can be used to apply a convolution  $\mathbf{M}_{\text{sk}} \otimes \mathbf{K}$  along the skeleton mask. We can then obtain all end pixels  $\mathbf{E}$  as pixels that have a value of 11 (1 neighbor) and all intersection pixels  $\mathbf{I}$  as pixels having a value greater than 12 (3 or more neighbors).

After obtaining both  $\mathbf{E}$  and  $\mathbf{I}$ , additional work must be done to obtain the correct representative sets. For example, end pixels that are unindicative of a topological end may be produced from a noisy binary mask. These “split ends” will then inadvertently produce intersection pixels themselves as shown in Fig. 2. Additionally, a single topological intersection will result in either two Y-shaped divides or a single X-shaped divide as shown in Fig. 3(a). Such pixels must be clustered together accordingly and a single point for the intersection must be determined. In the case of a skeleton possessing two Y-shaped divides in regards to a single intersection, the intersection must also be replaced with an X-shaped divide that more accurately represents the true centerlines of the DLOs. The next two sections will cover the pruning and clustering operations in detail.

#### D. Pruning Split Ends

When the boundary of the binary mask  $\mathbf{M}_{\text{dlo}}$  is jagged, the skeleton mask  $\mathbf{M}_{\text{sk}}$  may contain several types of split ends as shown in Fig. 2. Such split ends must be identified and pruned as they do not accurately represent the topology of the DLO(s) and will result in incorrect start points as well as cause path ambiguity during pixel traversals.

Note that the length of a split end can be at most the radius of the DLO it is sprouting from. Therefore, suffice it to say that the length of all split ends should be within a threshold  $\delta \ll \text{length of the DLO}$ . Given this, for every end in  $\mathbf{E}$ , we can traverse along its segment until 1 of 3 things may occur:

- 1) an intersection is encountered before traversing  $\delta$  pixels,
- 2) an end is encountered before traversing  $\delta$  pixels,
- 3) or neither was encountered after traversing  $\delta$  pixels.

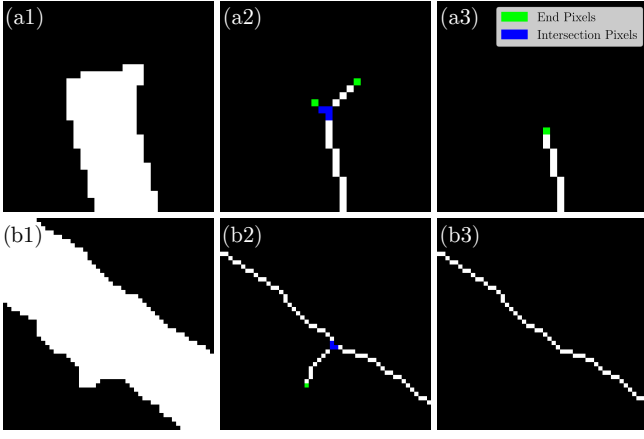


Fig. 2. Examples of split ends that may occur during the skeletonization process. Row (a) showcases split ends that may occur at an actual topological end, while row (b) showcases a split end along a segment produced by a jagged mask. For both examples, the first column shows the binary mask; the second column shows the split end after skeletonization, and the third column showcases the topologically correct structure after pruning.

For conditions (1) and (2), we remove the segment that was just traversed from  $M_{sk}$  as well as the corresponding end from  $E$ . For condition (1) specifically, we must also remove all intersection pixels that were produced from the pruned split end from  $I$ . For any endpoint that satisfies condition (3), we simply do nothing. This concludes eliminating any noise-induced end and intersection pixels.

#### E. Intersection Clustering and Replacement

As mentioned previously in Sec. III-C, a single topological intersection can result in either a 2Y or X-shaped branching as shown in Fig. 3(a). Furthermore, each of these branches may have several intersection pixels, i.e., pixels with 3 or more neighbors. Our goal then is to group each pixel in  $I$  to a single branch and then group each branch to its true topological intersection. With all the intersection pixels properly grouped, we can then define a single intersection pixel that represents the true center of a crossing for all crossings.

We perform clustering using Density-based Spatial Clustering of Applications with Noise (DBSCAN) [27], a clustering algorithm that clusters data points that are within a distance threshold  $\epsilon$  of each other. In our case,  $\epsilon$  will refer to Euclidean pixel distance. This algorithm is highly convenient to use as it does not necessitate prior knowledge of the number of clusters and thus, intersections.

To properly group all the intersection pixels in  $I$ , two phases of clustering are performed:

- 1) ( $\epsilon = 2$ ) All adjacent pixels in  $I$  are clustered together. Each cluster is then averaged create a new  $I$ .
- 2) ( $\epsilon > 2$ ) All pixels in the new  $I$  are clustered together with a higher  $\epsilon$ . This is to account for intersections that produced multiple Y-shaped branches. A new  $I$  is then created using the averages of the clusters like step 1.

This two step clustering process (shown in Fig. 3(b)) is crucial as skipping the first clustering step can result in the final center intersection pixel being heavily biased towards a

#### Algorithm 1: mBEST Pseudocode

---

**Input:**  $M_{dlo}, \delta, \epsilon$   
**Output:**  $P$

```

1 Func mBEST ( $M_{dlo}, \delta, \epsilon$ ) :
2    $P \leftarrow []$ 
3    $M_{sk} \leftarrow \text{Skeletonize}(M_{dlo})$ 
4    $E, I \leftarrow \text{DetectKeyPoints}(M_{sk} \otimes K)$ 
5    $E, I \leftarrow \text{PruneSplitEnds}(E, I, M_{sk}, \delta)$ 
6    $I \leftarrow \text{ClusterIntersections}(I, \epsilon)$ 
7    $P_{inter} \leftarrow \text{GenIntersectionPaths}(I, M_{sk})$ 
8   while  $E$  is not empty do
9      $x \leftarrow E.\text{pop}()$ 
10    while True do
11       $\tau \leftarrow \text{traverse along } M_{sk} \text{ from } x \text{ until}$ 
12         $\text{reaching an end } e$ 
13      if  $e \in P_{inter}$  then
14         $\tau \leftarrow \tau + P_{inter}^i$ 
15         $x \leftarrow \text{last pixel of } P_{inter}^i$ 
16      else
17         $E.\text{remove}(e)$ 
18        break
19       $P.\text{append}(\tau)$ 
20  return  $P$ 

```

---

particular branch. After the correct set of intersection pixels  $I$  is obtained, we can then replace all clustered Y-shaped branches with an X-shaped branch as shown in Fig. 3(c). This is done by simply removing all segments within a square window of the new intersection pixel and then creating new segments that sprout from the new intersection. Note that Fig. 3(c) shows that we record new “ends” when replacing the intersection. These ends are recorded so that we know that an intersection is upcoming during a pixel traversal. This allows us to then take the correct precomputed path, which is discussed in the next section.

#### F. Minimal Bending Energy Path Generation

For rods that have nonuniform curvatures, bending energy must be computed in a discretized fashion. Given this, if we discretize a rod into  $N$  nodes and  $N - 1$  edges, then the total bending energy becomes

$$E_b = \frac{1}{2} \frac{EI}{dl} \sum_{k=1}^{N-2} (\kappa_k - \kappa_k^0)^2, \quad (1)$$

where  $EI$  is the bending stiffness,  $\kappa_k$  and  $\kappa_k^0$  are the deformed and undeformed discrete dimensionless curvatures at node  $k \in [1, N - 2]$ , and  $dl$  is the Voronoi length. For our DLOs, we make the assumption that the undeformed curvature is always a straight configuration ( $\kappa^0 = 0$ ). It is then trivial to see that minimizing the bending energy of an elastic rod is the same as minimizing the discrete curvatures.

The norm of the discrete dimensionless curvature for a node  $k$  can easily be computed using the unit tangent vectors



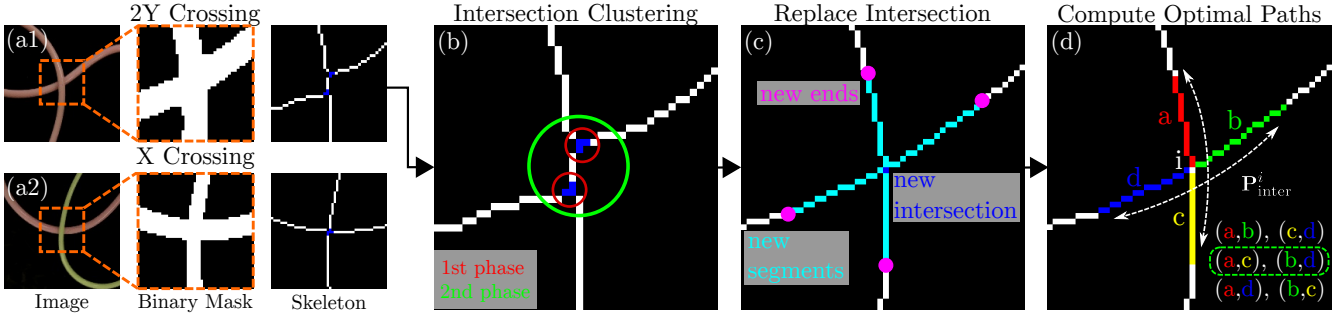


Fig. 3. The intersection clustering, replacement, and optimal path generation pipeline. Two sample intersections are shown where skeletonization results in a (a1) 2Y-shaped crossing and an (a2) X-shaped crossing. As 2Y-shaped crossings are topologically incorrect, we replace them by (b) clustering the intersection pixels in two stages. The first stage involves grouping adjacent pixels, while the second involves grouping nearby clusters. Using the centroid location of the cluster, we can then (c) replace the intersection by creating new ends and having new segments sprout and connect to the centroid. Finally, the new generated ends and segments can be used to (d) discover the combination of paths that minimizes the cumulative bending energy of the DLO.

of the adjacent edges [28]:

$$\bar{\kappa}_k = \left\| \frac{2\mathbf{t}^{k-1} \times \mathbf{t}^k}{1 + \mathbf{t}^{k-1} \cdot \mathbf{t}^k} \right\|, \quad (2)$$

where  $\mathbf{t}^{k-1}$  and  $\mathbf{t}^k$  are the unit tangent vectors of the  $k-1$ -th and  $k$ -th edges, respectively.

Note that the only time we have to choose between multiple paths is at an intersection as traversals through segments are unambiguous. Also recall that all intersections have been replaced with new segments in an X-shaped pattern. Using the new ends shown in Fig. 3(c), we can then compute the combination of paths that minimizes the cumulative bending energy of the DLOs using the optimization scheme

$$\begin{aligned} (\mathbf{p}_1^1, \mathbf{p}_1^2), (\mathbf{p}_2^1, \mathbf{p}_2^2) &= \arg \min_{\mathbf{a}, \mathbf{b}, \mathbf{c}, \mathbf{d}} \|\kappa_1\| + \|\kappa_2\|, \\ \mathbf{t}_1^1 &= \frac{\mathbf{i} - \mathbf{p}_1^1}{\|\mathbf{i} - \mathbf{p}_1^1\|}, \quad \mathbf{t}_1^2 = \frac{\mathbf{p}_1^2 - \mathbf{i}}{\|\mathbf{p}_1^2 - \mathbf{i}\|}, \\ \mathbf{t}_2^1 &= \frac{\mathbf{i} - \mathbf{p}_2^1}{\|\mathbf{i} - \mathbf{p}_2^1\|}, \quad \mathbf{t}_2^2 = \frac{\mathbf{p}_2^2 - \mathbf{i}}{\|\mathbf{p}_2^2 - \mathbf{i}\|}, \\ \kappa_1 &= \frac{2\mathbf{t}_1^1 \times \mathbf{t}_1^2}{1 + \mathbf{t}_1^1 \cdot \mathbf{t}_1^2}, \quad \kappa_2 = \frac{2\mathbf{t}_2^1 \times \mathbf{t}_2^2}{1 + \mathbf{t}_2^1 \cdot \mathbf{t}_2^2}, \end{aligned} \quad (3)$$

where  $\mathbf{i}$  is the intersection pixel and  $(\mathbf{a}, \mathbf{b}, \mathbf{c}, \mathbf{d})$  are the new recorded ends from the intersection replacement. A visual example of this optimization can be seen in Fig. 3(d) where out of the 3 possible combinations of paths, the one that minimizes total curvature is selected. With the paths through intersections properly precomputed, the skeleton pixel traversals to obtain each DLO's centerline can now take place. Pseudocode pertaining to the full pipeline can be seen in Alg. 1.

#### G. Computing DLO Radii and Crossing Order

The final step of the pipeline concerns computing the pixel radii of the DLOs (to create the optional segmentation masks) as well as ascertaining which DLO is resting on top of the other at intersections. To solve both problems, we use modified versions of *FASTDLO*'s solutions [14].

Similar to *FASTDLO*, to compute the radii of the DLOs, we first perform a distance transform on the binary mask

$\mathbf{M}_{\text{dlo}}$ , which results in a new mask  $\mathbf{M}_{\text{dist}}$  containing the closest distance to a 0-value pixel. Diverting from *FASTDLO*, we then use the average distance value of  $\mathbf{M}_{\text{dist}}$  along a DLO's centerline as the radius of that DLO when creating segmentation masks. Using the average in this manner allows for smooth segmentations even if the initial binary mask itself is noisy. For segments of the DLO near the edges of the image, we use the pixel specific values of  $\mathbf{M}_{\text{dist}}$  themselves.

To compute crossing order at intersections, we use the precomputed optimal paths created in Fig. 3(d). Crossing order can then be determined by computing the sum of the standard deviations of the RGB channels of the pixels along each path. The path that contains the lower sum is then assumed to be the one on top. Though this solution from *FASTDLO* works fairly well, we noticed that failures could occur due to glare along the centerline. This glare issue could even cause failures for intersections with two completely different colored DLOs. Therefore, to eliminate the influence of glare, we compute the standard deviations of the intersection path pixels on a blurred image, rather than the original input image.

## IV. EXPERIMENTAL RESULTS

### A. Experiments and Datasets

We conduct a total of 3 experiments using two datasets. The first experiment consists of segmenting a dataset of 10 images from [14] where a series of wires can be seen against complex backgrounds. Though the background is complex, the wires themselves possess relatively smooth curvatures and no self-loops. For this “complex background” dataset, the DLO segmentation method used is *FASTDLO*'s DCNN model. Ground truth images for the complex background dataset are created using the photo editing software Photopea [29].

The second and third experiments consists of segmenting a dataset of 50 images consisting of up to two uniquely colored elastic rods against a simple black background using DCNN and color filter segmentation, respectively. Using both methods lets us observe the effects of the initial DLO segmentation on overall performance. This “simple background” dataset consists of DLOs with highly varying

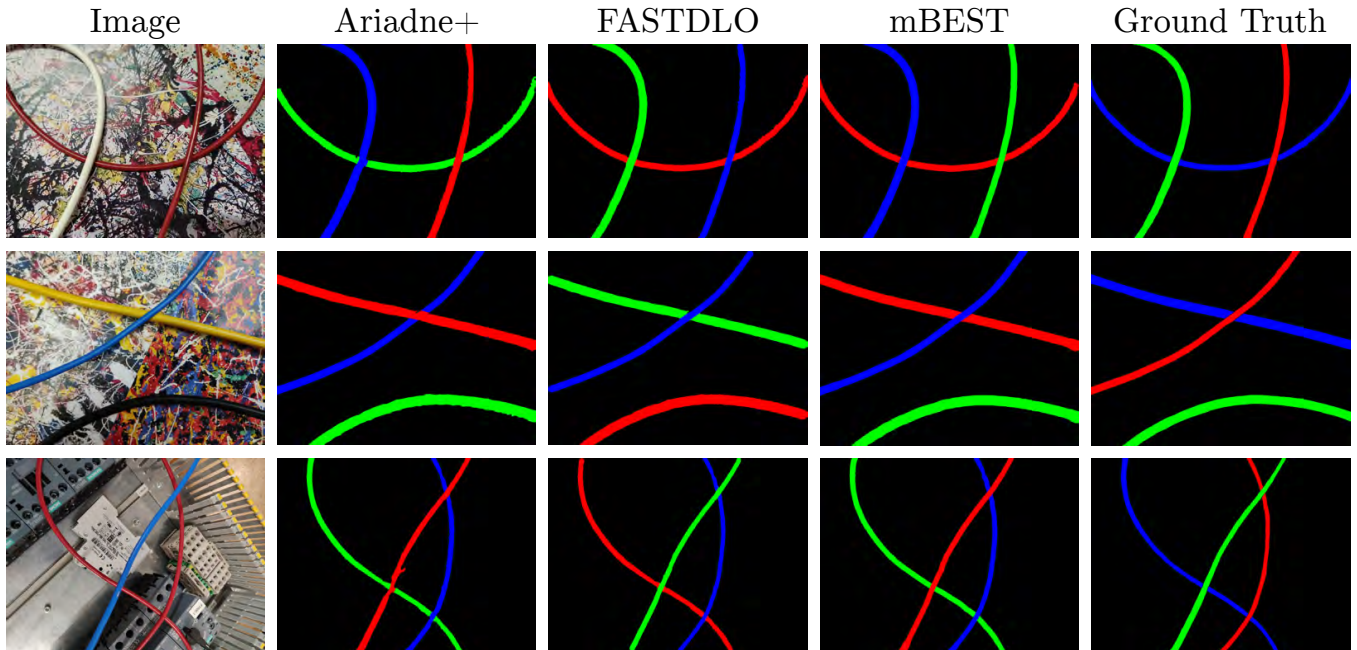


Fig. 4. Sample segmentations for the complex background dataset. Each row showcases segmentation results for a different image. From left to right, the first column showcases the original image. Columns 2-4 showcase *Ariadne+*, *FASTDLO*, and *mBEST* results, respectively. Finally, the fifth column showcases ground truth.

TABLE II  
EXPERIMENTAL RESULTS WITH DICE METRIC AND AVERAGE RUNTIME

Dataset	Segmentation Type	Image Size	DICE (%)			Average Runtime (FPS)		
			<i>Ariadne+</i>	<i>FASTDLO</i>	<i>mBEST</i>	<i>Ariadne+</i>	<i>FASTDLO</i>	<i>mBEST</i>
Complex background	DCNN	1000 × 750	85.39	83.93	<b>85.66</b>	0.96	6.88	<b>11.48</b>
Simple background	DCNN	672 × 896	80.53	69.00	<b>81.67</b>	0.76	8.23	<b>15.00</b>
Simple background	Color	672 × 896	93.87	79.84	<b>95.61</b>	0.73	14.76	<b>39.32</b>

curvatures and numerous self-loops. Ground truth images for the simple background dataset are created simply using the color filters themselves. We focus mostly on images with a simple black background since the initial binary mask segmentation is not a key focus of our algorithm. Having said this, we show that *mBEST* still works for complex backgrounds in Fig. 6. All experiments were run using an Intel i9-9900KF CPU and an NVIDIA RTX 2080 Ti GPU.

### B. Baselines and Parameters

We test our algorithm against two state-of-the-art baselines: *Ariadne+* [25] and *FASTDLO* [14]. For complex background images, the number of superpixels for *Ariadne+* was set to 75, while simple background images used 200 superpixels. Both these values were chosen as optimal after performing a parameter sweep on each dataset.

For all experiments involving using the DCNN model, a pixel segmentation threshold of 50 and 77 (0-255) were used for the simple and complex backgrounds, respectively. Furthermore, though *Ariadne+* has its own neural network for initial segmentation of the DLOs, we exchange this for *FASTDLO*'s DCNN model for consistency as well as the latter's model having better performance. Parameters

for *mBEST* involve an intersection clustering threshold of  $\epsilon = 75$  and minimum pixel length threshold of  $\delta = 40$  for complex background images. For simple background images, ( $\epsilon = 45, \delta = 25$ ) and ( $\epsilon = 40, \delta = 25$ ) were used for segmentations with DCNN and color filtering, respectively.

### C. Results

For experiments, we report two key metrics. First, we look at segmentation accuracy using the popular metric DICE. As all methods share the same initial segmentation method for creating the binary mask, we do not treat the background as one of the classes when computing the DICE scores. In addition to this, we also report the average run times for each algorithm in terms of frames per second (FPS). Both metrics can be seen listed in Table II for all experiments.

Fig. 4 showcases results for the complex background dataset. For this dataset, all three algorithms have relatively similar performance with *mBEST* slightly edging out the others. As this dataset was originally used to evaluate *FASTDLO*, it comes as no surprise that all three algorithms perform well, especially since the configurations of the DLOs themselves are quite simple. Though segmentation accuracy between the algorithms are similar, *mBEST* achieves roughly a

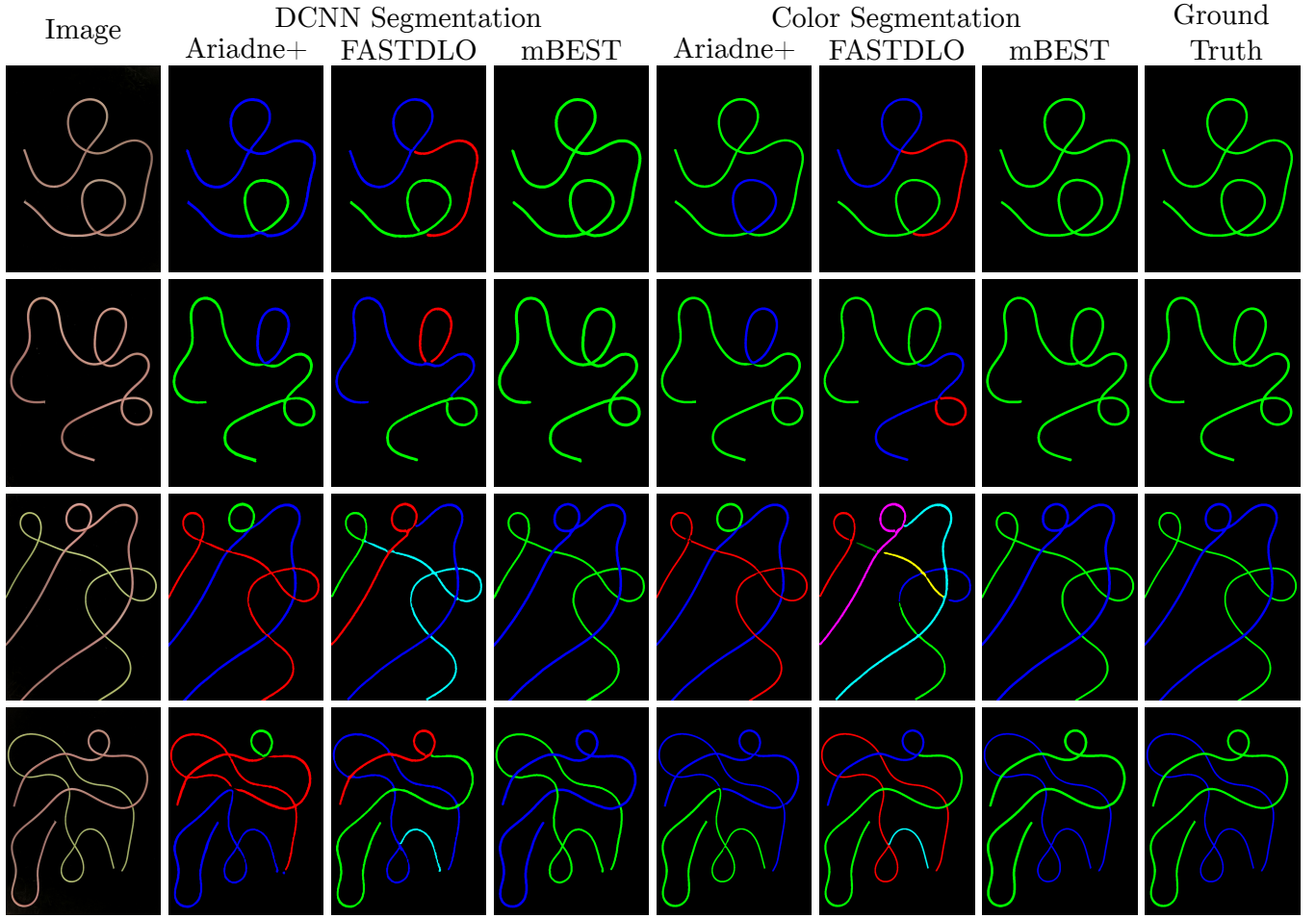


Fig. 5. Sample segmentations for the simple background dataset. Each row showcases segmentation results for a different image. From left to right, the first column showcases the original image. Columns 2-4 showcase results for *Ariadne+*, *FASTDLO*, and *mBEST* using DCNN segmentation, respectively. Columns 5-7 do the same except with color filter segmentation. Finally, ground truth can be seen in the last column.

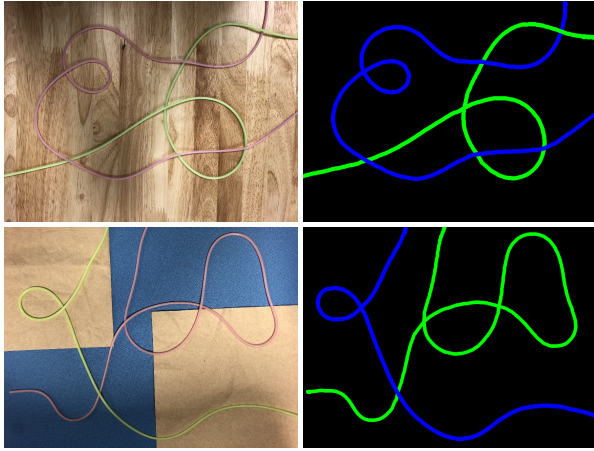


Fig. 6. Examples of *mBEST* with DCNN segmentation working for scenes with complex DLO configurations and backgrounds.

12 $\times$  runtime improvement over *Ariadne+* and 1.67 $\times$  runtime improvement over *FASTDLO*.

Where we start to see a large improvement in performance is the images containing complex configurations of DLOs

as shown in Fig. 5. For these images, *mBEST* and *Ariadne+* significantly outperform *FASTDLO* when using both DCNN and color filtering approaches, with *mBEST* slightly beating the latter. We suspect that *Ariadne+*'s use of curvature as one of its neural network inputs helps it keep up with *mBEST*. Despite this, we can see that *Ariadne+* is still susceptible to choosing incorrect paths when encountering intersections with high curvatures as shown in various examples in Fig. 5. In terms of runtime, we see that *mBEST* has up to 2.66 $\times$  speed boost over *FASTDLO* and up to a staggering 53.86 $\times$  speed boost over *Ariadne+* when using color filtering. These improvements decrease when using the DCNN model which indicates that the DCNN passthrough takes a significant amount of computation time on its own. Overall, we show that our physically insightful intersection handling scheme can lead to more robust results when compared to blackbox neural networks.

#### D. Failure Cases

Though *mBEST* performs quite well for detecting complex tangles, it is still reliant on correctly setting  $\epsilon$ . Improperly setting  $\epsilon$  by even a few pixels can result in improper handling



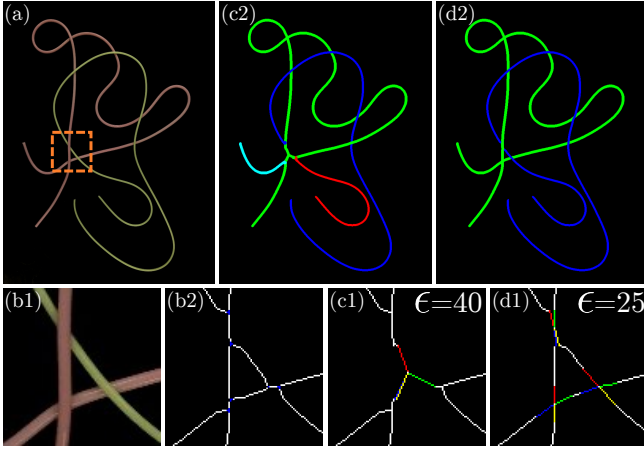


Fig. 7. Example of a failure caused by inadequate selection of the intersection clustering threshold  $\epsilon$ . (a) showcases the original image where the orange dashed box encloses a (b1) set of three closely packed intersections. (b2) showcases the skeleton pixel structure of the intersections. (c1-c2) showcases the intersections improperly being replaced when  $\epsilon$  is set too high, while (d1-d2) showcases the intersections properly handled.

of intersections as shown in Fig. 7 where  $\epsilon = 40$  results in several topological intersections being incorrectly clustered as one. Removing this hyperparameter reliance will be a focus in future works.

## V. CONCLUSION

In this work, we have introduced *mBEST*, an end-to-end pipeline for DLO segmentation that improves upon SOTA in both accuracy and computational speed. Through a wide variety of experiments, we have shown that *mBEST* can robustly handle scenes with highly tangled DLOs by simply generating paths that minimize cumulative bending energy. For future work, we would like to explore solutions that take into consideration occlusions, strands touching in parallel, and removing the hyperparameter dependency of  $\epsilon$ .

## REFERENCES

- [1] J. Sanchez, J.-A. Corrales, B.-C. Bouzgarrou, and Y. Mezouar, "Robotic manipulation and sensing of deformable objects in domestic and industrial applications: a survey," *The International Journal of Robotics Research*, vol. 37, no. 7, pp. 688–716, 2018.
- [2] J. Schulman, A. Gupta, S. Venkatesan, M. Tayson-Frederick, and P. Abbeel, "A case study of trajectory transfer through non-rigid registration for a simplified suturing scenario," in *2013 IEEE/RSJ International Conference on Intelligent Robots and Systems*, pp. 4111–4117, IEEE, 2013.
- [3] H. Mayer, F. Gomez, D. Wierstra, I. Nagy, A. Knoll, and J. Schmidhuber, "A system for robotic heart surgery that learns to tie knots using recurrent neural networks," *Advanced Robotics*, vol. 22, no. 13-14, pp. 1521–1537, 2008.
- [4] A. Choi, D. Tong, M. K. Jawed, and J. Joo, "Implicit contact model for discrete elastic rods in knot tying," *Journal of Applied Mechanics*, vol. 88, no. 5, 2021.
- [5] J. Zhu, B. Navarro, P. Fraisse, A. Crosnier, and A. Cherubini, "Dual-arm robotic manipulation of flexible cables," in *2018 IEEE/RSJ International Conference on Intelligent Robots and Systems (IROS)*, pp. 479–484, IEEE, 2018.
- [6] M. Yu, H. Zhong, and X. Li, "Shape control of deformable linear objects with offline and online learning of local linear deformation models," in *2022 International Conference on Robotics and Automation (ICRA)*, pp. 1337–1343, IEEE, 2022.

- [7] J. Iqbal, Z. H. Khan, and A. Khalid, "Prospects of robotics in food industry," *Food Science and Technology*, vol. 37, pp. 159–165, 2017.
- [8] D. Tong, A. Borum, and M. K. Jawed, "Automated stability testing of elastic rods with helical centerlines using a robotic system," *IEEE Robotics and Automation Letters*, vol. 7, no. 2, pp. 1126–1133, 2021.
- [9] B. Audoly, N. Clauvelin, and S. Neukirch, "Elastic knots," *Physical Review Letters*, vol. 99, no. 16, p. 164301, 2007.
- [10] M. K. Jawed, P. Dieleman, B. Audoly, and P. M. Reis, "Untangling the mechanics and topology in the frictional response of long overhand elastic knots," *Physical review letters*, vol. 115, no. 11, p. 118302, 2015.
- [11] V. P. Patil, J. D. Sandt, M. Kolle, and J. Dunkel, "Topological mechanics of knots and tangles," *Science*, vol. 367, no. 6473, pp. 71–75, 2020.
- [12] P. Johanns, P. Grandgeorge, C. Baek, T. G. Sano, J. H. Maddocks, and P. M. Reis, "The shapes of physical trefoil knots," *Extreme Mechanics Letters*, vol. 43, p. 101172, 2021.
- [13] T. G. Sano, P. Johanns, P. Grandgeorge, C. Baek, and P. M. Reis, "Exploring the inner workings of the clove hitch knot," *Extreme Mechanics Letters*, p. 101788, 2022.
- [14] A. Caporali, K. Galassi, R. Zanella, and G. Palli, "Fastdlo: Fast deformable linear objects instance segmentation," *IEEE Robotics and Automation Letters*, vol. 7, no. 4, pp. 9075–9082, 2022.
- [15] A. Keipour, M. Bandari, and S. Schaal, "Deformable one-dimensional object detection for routing and manipulation," *IEEE Robotics and Automation Letters*, vol. 7, no. 2, pp. 4329–4336, 2022.
- [16] M. Yan, Y. Zhu, N. Jin, and J. Bohg, "Self-supervised learning of state estimation for manipulating deformable linear objects," *IEEE robotics and automation letters*, vol. 5, no. 2, pp. 2372–2379, 2020.
- [17] D. De Gregorio, G. Palli, and L. Di Stefano, "Let's take a walk on superpixels graphs: Deformable linear objects segmentation and model estimation," 2018.
- [18] D. Bolya, C. Zhou, F. Xiao, and Y. J. Lee, "Yolact: Real-time instance segmentation," in *Proceedings of the IEEE/CVF international conference on computer vision*, pp. 9157–9166, 2019.
- [19] D. Bolya, C. Zhou, F. Xiao, and Y. J. Lee, "Yolact++: Better real-time instance segmentation," *IEEE transactions on pattern analysis and machine intelligence*, 2020.
- [20] H. Chen, K. Sun, Z. Tian, C. Shen, Y. Huang, and Y. Yan, "Blendmask: Top-down meets bottom-up for instance segmentation," in *Proceedings of the IEEE/CVF conference on computer vision and pattern recognition*, pp. 8573–8581, 2020.
- [21] Z. Tian, C. Shen, and H. Chen, "Conditional convolutions for instance segmentation," in *European conference on computer vision*, pp. 282–298, Springer, 2020.
- [22] M. Denninger, M. Sundermeyer, D. Winkelbauer, Y. Zidan, D. Olefir, M. Elbadrawy, A. Lodhi, and H. Katam, "Blenderproc," *arXiv preprint arXiv:1911.01911*, 2019.
- [23] W. Qiu and A. Yuille, "Unrealcv: Connecting computer vision to unreal engine," in *European Conference on Computer Vision*, pp. 909–916, Springer, 2016.
- [24] R. Zanella, A. Caporali, K. Tadaka, D. De Gregorio, and G. Palli, "Auto-generated wires dataset for semantic segmentation with domain-independence," in *2021 International Conference on Computer, Control and Robotics (ICCCR)*, pp. 292–298, IEEE, 2021.
- [25] A. Caporali, R. Zanella, D. D. Gregorio, and G. Palli, "Ariadne+: Deep learning-based augmented framework for the instance segmentation of wires," *IEEE Transactions on Industrial Informatics*, vol. 18, no. 12, pp. 8607–8617, 2022.
- [26] T. Y. Zhang and C. Y. Suen, "A fast parallel algorithm for thinning digital patterns," *Commun. ACM*, vol. 27, p. 236, mar 1984.
- [27] M. Ester, H.-P. Kriegel, J. Sander, and X. Xu, "A density-based algorithm for discovering clusters in large spatial databases with noise," in *Knowledge Discovery and Data Mining*, 1996.
- [28] M. Bergou, M. Wardetzky, S. Robinson, B. Audoly, and E. Grinspun, "Discrete elastic rods," in *ACM SIGGRAPH 2008 Papers, SIGGRAPH '08*, (New York, NY, USA), Association for Computing Machinery, 2008.
- [29] "Photopea." <https://www.photopea.com/>.